Journal of Materials Chemistry A

RSC Publishing

PAPER

View Article Online
View Journal | View Issue

Cite this: J. Mater. Chem. A, 2013, 1, 1185

Surface-coordination-induced selective synthesis of cubic and orthorhombic $NaNbO_3$ and their photocatalytic properties†

Peng Li,[abc] Shuxin Ouyang,[b] Yuanjian Zhang,[c] Tetsuya Kako[ab] and Jinhua Ye*[abcd]

Received 11th September 2012
Accepted 30th October 2012

DOI: 10.1039/c2ta00260d

www.rsc.org/MaterialsA

$NaNbO_3$ photocatalysts with cubic and orthorhombic structures were selectively fabricated at a low temperature using different starting reagents through a surface coordination modulation. The samples were characterized by X-ray diffraction, field emission-transmission electron microscopy, ultraviolet-visible absorption spectroscopy and Fourier transform infrared spectroscopy. A surface ligand coordination effect is proposed to understand the crystal growth mechanism of cubic $NaNbO_3$. Induced by the organic ligands, cubic $NaNbO_3$ could be prepared at a temperature as low as 500 °C. Interestingly, the as-synthesized cubic $NaNbO_3$ shows better photocatalytic performances than those prepared at temperatures over 600 °C by the conventional way, both in H_2 evolution from methanol aqueous solution and CO_2 photoreduction in the gas phase. The enhanced photocatalytic activities could be attributed to the preferred crystal structure induced by the surface ligand coordination and the larger surface area obtained from the low formation temperature.

Introduction

Since it was reported that water could be split into H_2 and O_2 over a TiO_2 photoanode under a small applied bias upon UV light irradiation in 1971,[1] the efficient conversion of solar energy into chemical energy using semiconductors has attracted particular interest. In this regard, photocatalysis is among the best potential solutions for the global energy and environmental crisis.[2–4] In general, the photocatalytic performances of semiconductors are strongly affected by various parameters, including crystallinity, surface area, surface state and the most effective factor, the crystal phase.[5–7] For example, the effect of crystal and electronic structures on photocatalytic reactions has been studied for different crystal forms of TiO_2, CdS, $BiVO_4$ and $AgGaO_2$.[8–12] It was found that photocatalysts with different crystal structures show quite different photocatalytic performances.

As a promising photocatalyst, $NaNbO_3$ exhibits a sequence of temperature driven phase transitions.[13,14] Traditionally, the most stable phase of $NaNbO_3$ at room temperature is orthorhombic with the space group *Pbcm*, while the cubic phase with the space group $Pm\bar{3}m$ exists only at high temperature (>913 K).[15,16] $NaNbO_3$ was reported as an excellent photocatalyst in water splitting and CO_2 reduction.[17–20] For instance, cubic $NaNbO_3$ was synthesized by a furfural alcohol-derived polymerization–oxidation (FAPO) method, and cubic $NaNbO_3$ shows better photocatalytic performances than orthorhombic $NaNbO_3$.[21] The photocatalytic reactions over $NaNbO_3$ are particularly affected by the crystal structure because of the specific crystal and electronic structures of cubic $NaNbO_3$, which benefit the electron excitation and the charge carrier migration.[21] However, the high-temperature calcination, which was commonly used to remove the organic compounds in the FAPO synthesis, always resulted in a small surface area.[22] To improve the crystal growth controllability for a particular crystal phase and large surface area, many surface ligands were employed as the additives or surfactants in the material preparation.[23,24] The formation of cubic $NaNbO_3$ in the FAPO synthesis is probably induced by the surface coordination effect. Thus, we speculated that it is possible to control the crystal structure of $NaNbO_3$ by adjusting the surface ligands.

In this study, cubic and orthorhombic $NaNbO_3$ were selectively synthesized by using different surface ligands according to the surface coordination effect. The formation mechanism of cubic $NaNbO_3$ was investigated by Fourier transform infrared

[a]Department of Chemistry, Graduate School of Science, Hokkaido University, Sapporo, Japan

[b]Catalytic Materials Group, Environmental Remediation Materials Unit, National Institute for Materials Science (NIMS), 1-1 Namiki, Tsukuba, Ibaraki 305-0047, Japan. E-mail: Jinhua.YE@nims.go.jp

[c]International Center for Materials Nanoarchitectonics (WPI-MANA), National Institute for Materials Science (NIMS), 1-1 Namiki, Tsukuba, Ibaraki, Japan

[d]TU-NIMS Joint Research Center, School of Materials Science and Engineering, Tianjin University, 92 Weijin Road, Nankai District, Tianjin, P. R. China

† Electronic supplementary information (ESI) available: The Raman spectra of $NaNbO_3$–inorganic and $NaNbO_3$–organic. GC-MS spectra of $^{13}CO_2$ reduction products. The mobility distributions of $NaNbO_3$–inorganic and $NaNbO_3$–organic precursor colloidal particles. XRD patterns of the low temperature oxidation samples of $NaNbO_3$–inorganic and $NaNbO_3$–organic. See DOI: 10.1039/c2ta00260d

(FT-IR), X-ray diffraction (XRD) and ζ potential measurements. A surface-coordination induced growth process was also proposed to understand the chemical composition during the synthesis. Finally, we continued to optimize the oxidation temperature so that cubic $NaNbO_3$ photocatalyst could be obtained at a lower oxidation temperature to achieve the enhanced activities in photocatalytic H_2 evolution and CO_2 reduction.

Experimental

Material preparation

The organic coordinated $NaNbO_3$ samples were synthesized through a FAPO process.[21,25] Firstly, 1.0 g $(C_2H_5O)_5Nb$ and 0.24 g C_2H_5ONa were dissolved in 15 mL 2-methoxyethanol and the solution was stirred for 30 min to form a clear colloid. Then, 30 mL 2-methoxyethanol solution containing 2.5 g P-123 (M_w = 5800) was added. After being stirred for 30 min, the mixture was heated to 120 °C and maintained at this temperature for 120 h to form a solid precursor. Finally, the precursor was oxidized in air at 500–900 °C for 10 h and a white powder product was obtained.

The inorganic coordinated $NaNbO_3$ sample was synthesized by the FAPO method and the starting reagents were different from the synthesis of the organic coordinated sample. Firstly, 1.0 g $NbCl_5$ was dissolved in 15 mL 2-methoxyethanol and the solution was stirred for 30 min until a colourless transparent solution was obtained. Then, 0.21 g Na_2CO_3 was added and the solution was continually stirred for 12 h to form a clear colloid. Next, 30 mL 2-methoxyethanol solution containing 2.5 g P-123 (M_w = 5800) was added. After being stirred for 30 min, the mixture was heated to 120 °C and maintained at this temperature for 120 h to form a solid precursor. Finally, the precursor was oxidized in air at 600 °C for 10 h and a white powder product was obtained.

Sample characterization

The crystal structures of $NaNbO_3$ samples were determined with an X-ray diffractometer (Rint-2000, Rigaku Co., Japan) with Cu-Kα radiation. Transmission electron microscopy (TEM) and high-resolution images were recorded with a field-emission transmission electron microscope (2100F, JEOL Co., Japan) operated at 200 kV. The diffuse reflection spectra were measured with an integrating sphere equipped ultraviolet-visible (UV-visible) recording spectrophotometer (UV-2500PC, Shimadzu Co., Japan) using $BaSO_4$ as reference and the optical absorption spectra were converted from the diffuse reflection spectra according to the Kubelka–Munk equation. A Fourier transform-infrared (FT-IR) spectrophotometer (IR Prestige-21, Shimadzu Co., Japan) was utilized to obtain IR absorption spectra. The specific surface areas were determined with a surface-area analyzer (BEL Sorp-II mini, BEL Japan Co., Japan) by the Brunauer–Emmett–Teller (BET) method. The ζ potentials were measured with a ζ potential & particle size analyzer (Delsa Nano C, Beckman Coulter Inc., U. S. A.).

Photocatalytic H_2 evolution

The H_2 evolution experiments were carried out in a gas-closed circulation system. The $NaNbO_3$ powder (0.3 g) was dispersed using a magnetic stirrer in CH_3OH aqueous solution (220 mL distilled water + 50 mL CH_3OH) in a Pyrex cell with a side window. Then 0.5 wt% of Pt co-catalyst was photodeposited on the $NaNbO_3$ catalyst by adding H_2PtCl_6 solution to the reaction solution. The light source was a 300 W Xe arc lamp without filter. The H_2 evolution was measured by an on-line gas chromatograph (GC-8A, Shimadzu Co., Japan) with a thermal conductivity detector (TCD), according to the standard curve. After the H_2 evolution persisted for 8 h, the resulting $NaNbO_3$ powder was collected by centrifugation and washed with distilled water several times. Then the sample was dried at 70 °C and continually heated at 400 °C for 3 h to remove the organic compounds adsorbed on the surface of the catalyst. The obtained sample with 0.5 wt% Pt-loading was further used for the photoactivity measurement of CO_2 reduction.

CO_2 photoreduction

The CO_2 photoreduction experiments were carried out in a gas-closed circulation system. The $NaNbO_3$ powder with 0.5 wt% Pt-loading (0.1 g) was dispersed in a glass cell (8.0 cm^2) and then located in a Pyrex reaction cell equipped with a window on the top. After that, 3.0 mL distilled water was added into the gas-closed reaction system. Then, the whole system was evacuated and filled with 80 kPa pure CO_2 gas. The light source was a 300 W Xe arc lamp without filter. The organic product was sampled and measured by a gas chromatograph (GC-14B, Shimadzu Co., Japan) equipped with a flame ionization detector (FID), according to the standard curve.

Results and discussion

Selective synthesis of cubic and orthorhombic $NaNbO_3$

The crystallographic phases of the $NaNbO_3$ samples prepared with organic starting reagents ($NaNbO_3$–organic) and inorganic starting reagents ($NaNbO_3$–inorganic) at 600 °C were studied by X-ray diffraction (XRD) (Fig. 1). The $NaNbO_3$–organic and

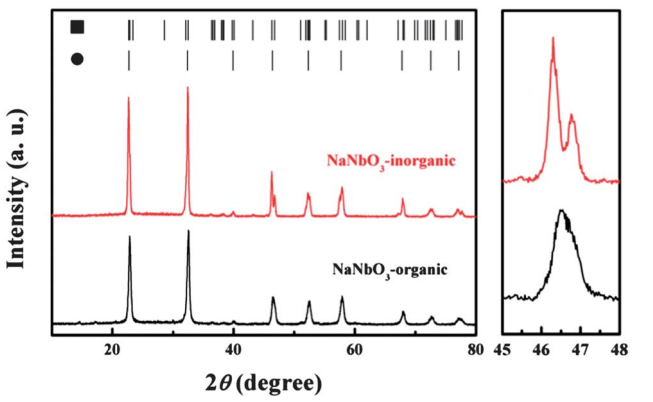

Fig. 1 XRD patterns of $NaNbO_3$–inorganic and $NaNbO_3$–organic (■: orthorhombic; ●: cubic).

$NaNbO_3$–inorganic samples are crystallized in cubic and orthorhombic phases, respectively (Table 1). All the peaks in the patterns could be indexed to the standard database (JCPDS-075-2102 for cubic $NaNbO_3$ and JCPDS-073-0803 for orthorhombic $NaNbO_3$). The phase difference is evident in the (200) diffraction peak of cubic $NaNbO_3$ where 2θ is about 46.5°. The $NaNbO_3$–organic sample has one symmetric diffraction peak, while the $NaNbO_3$–inorganic sample has a shoulder peak in the XRD pattern. The two diffraction peaks of $NaNbO_3$–inorganic are separated by 0.5° which is evidently distinguished from the separation of $K\alpha_1$ and $K\alpha_2$ (0.12°). The average crystallite sizes of $NaNbO_3$–organic and $NaNbO_3$–inorganic were calculated to be 22 and 31 nm, respectively, using the Debye–Scherrer equation.

Transmission electron microscopy (TEM) and high-resolution transmission electron microscopy (HR-TEM) were further used to investigate the crystal differences between the two samples. The TEM images in Fig. 2 suggest that no matter which kind of starting reagent was used in the preparation, the $NaNbO_3$ crystallite always grew into cuboid particles. The same morphology of the two samples should be attributed to the effect of P123 and the furfural alcohol polymerization. Nevertheless, the two samples have obviously different particle sizes. The $NaNbO_3$–organic sample contains particles with a size of about 30 nm, while particles with a size of about 50 nm constitute the $NaNbO_3$–inorganic sample. As exhibited in Fig. 2c, two sets of orthorhombic fringes with lattice spacings of 5.50 Å and 5.57 Å are observed from the $NaNbO_3$–inorganic sample, corresponding to the {100} and {010} planes of orthorhombic $NaNbO_3$, respectively. From Fig. 2d, the $NaNbO_3$–organic sample exhibits two mutually perpendicular fringes with the same *d*-spacing, 3.90 Å, which could be indexed to the {010} and {100} planes of cubic $NaNbO_3$. More evidence that distinguishes the two phases of $NaNbO_3$ could also be found from the Raman spectra (Fig. S1 in ESI†). The surface areas of $NaNbO_3$–organic and $NaNbO_3$–inorganic are measured to be 27.5 and 22.1 $m^2\ g^{-1}$, respectively, which are in agreement with the crystallite size calculations from the XRD patterns and the observations from the TEM images.

The surface conditions of the $NaNbO_3$–organic and $NaNbO_3$–inorganic samples are studied by FT-IR measurements. In the IR spectra (Fig. 3a), both $NaNbO_3$–organic and $NaNbO_3$–inorganic have strong absorptions at about 950 cm^{-1}, which belong to the stretching vibrations of Nb–O bonds. No evident peak belonging to C–H vibration is found in the range of 2800–3000 cm^{-1}, which means that the organic materials were completely oxidized during the 10 hour calcination. In the range above 2000 cm^{-1}, there is no distinguishable absorption. The significant differences exist in the range from 1200 to 1800 cm^{-1}. Previous investigations revealed that the absorption peaks at 1340, 1523 and 1655 cm^{-1}, which are momentously higher in the spectrum of $NaNbO_3$–organic, should be attributed to the absorptions of carbonate ions.[26,27] The absorptions of carbonate ions appearing in the spectrum of $NaNbO_3$–inorganic are possibly generated from the remaining carbonate on the surface, which was produced by the oxidation of the organic compounds.

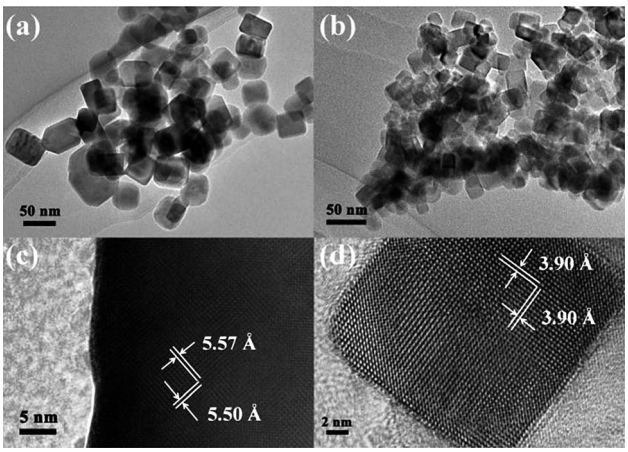

Fig. 2 TEM images of (a) $NaNbO_3$–inorganic and (b) $NaNbO_3$–organic. HR-TEM images of (c) $NaNbO_3$–inorganic and (d) $NaNbO_3$–organic.

Fig. 3b displays the UV-visible absorption spectra of the $NaNbO_3$–organic and $NaNbO_3$–inorganic powder samples. Both of the samples are merely responsive to the UV light and have sharp absorption edges. Compared with $NaNbO_3$–organic, the absorption edge of $NaNbO_3$–inorganic has a slight blue shift, suggesting that $NaNbO_3$–organic could absorb photons with lower energy. The band gaps (E_g) of $NaNbO_3$–organic and $NaNbO_3$–inorganic were determined by the following equation

$$(\alpha h\nu)^n = A(h\nu - E_g)$$

in which α, ν, A and E_g are the absorption coefficient, light frequency, proportionality constant and band gap, respectively.[28] The value of index n depends on the property of the material: whereas $n = 2$ for the direct band-gap semiconductors, $n = 1/2$ for the indirect band-gap semiconductors. For the $NaNbO_3$ samples, the index n was determined to be 1/2 according to the relationship between $\lg(\alpha h\nu)$ and $\lg(h\nu - E_g)$. From the inset of Fig. 3b, the band gaps of $NaNbO_3$–organic and $NaNbO_3$–inorganic are determined to be 3.25 and 3.40 eV, respectively.

Table 1 Crystal structures of $NaNbO_3$–organic and $NaNbO_3$–inorganic

Material	Crystal system	Lattice parameters (Å)	Surface area ($m^2\ g^{-1}$)
$NaNbO_3$–organic	Cubic	$a = 3.897(1)$	27.5
$NaNbO_3$–inorganic	Orthorhombic	$a = 5.515(1)$ $b = 5.572(1)$ $c = 15.525(2)$	22.1

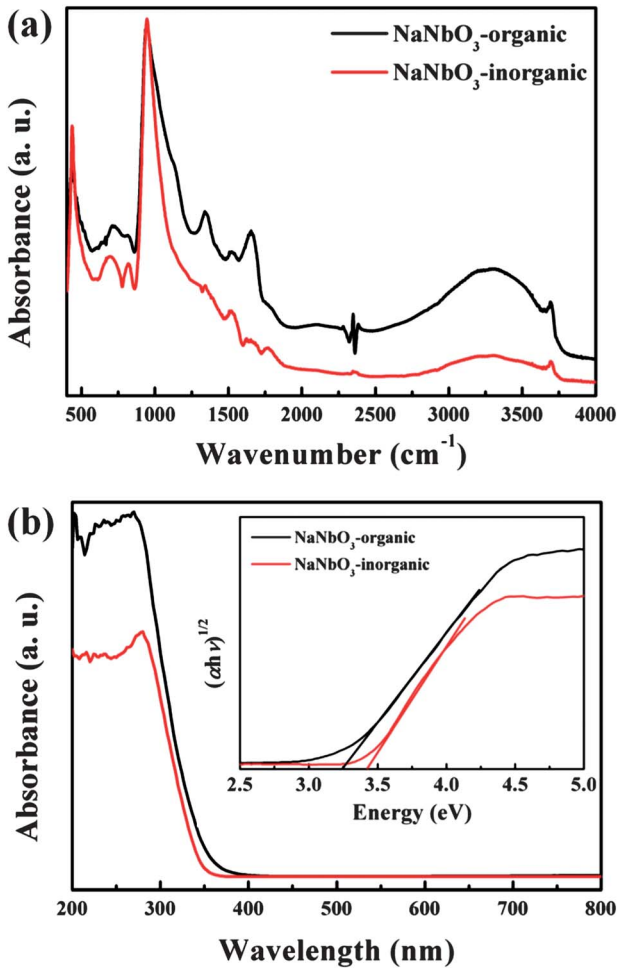

Fig. 3 (a) FT-IR spectra and (b) UV-vis absorption spectra of $NaNbO_3$–inorganic and $NaNbO_3$–organic. The inset in figure (b) shows the corresponding $(\alpha h\nu)^{1/2} \sim h\nu$ curves.

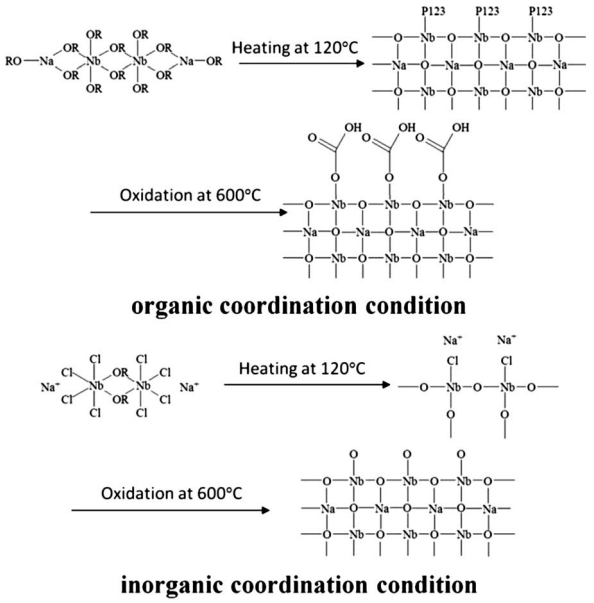

Scheme 1 The formation mechanisms of cubic and orthorhombic $NaNbO_3$ with organic and inorganic coordination, respectively.

To understand the formation mechanisms of cubic and orthorhombic $NaNbO_3$, different surface coordination processes in the synthesis (as shown in Scheme 1) are proposed. Firstly, with the organic starting reagents ($Nb(OC_2H_5)_5$ and $NaOC_2H_5$), the Nb^{5+} and Na^+ ions are coordinated by the $CH_3OC_2H_4O^-$ group based on the alcohol exchange reaction and a coordination network is formed when $Nb(OC_2H_5)_5$ and $NaOC_2H_5$ are dissolved in $CH_3OC_2H_4OH$.[29] Secondly, the $CH_3OC_2H_4O^-$ groups, which are coordinated to the surface of this network, are replaced by P123 molecules after the furfural alcohol solution containing P123 is added. Thirdly, in the process of polymerization, the coordination networks are separated by the polymerized furfuryl alcohol. Fourthly, the $CH_3OC_2H_4O^-$ groups, P123 and polymerized furfuryl alcohol are oxidized in sequence, which is proved by the TGA measurement. The typical evidence of the surface coordination is that when the P123 molecules are oxidized to CO_2, the carbonate ions might be left on the surface of the product. The carbonate ions coordinated to the $NaNbO_3$ surface lower the surface energy of $NaNbO_3$, which induces the formation of the cubic $NaNbO_3$ crystals. However, when the starting reagents are changed to $NbCl_5$ and Na_2CO_3, the first step is to form the $NbCl_x(OC_2H_4OCH_3)_{5-x}$ complex.[30] Then, the Na^+ ions are adsorbed onto the complex surface to generate the colloidal particle by the electrostatic interaction. The ζ potential of this colloidal solution is -28.38 mV, while the ζ potential of the colloidal solution prepared by $Nb(OC_2H_5)_5$ and $NaOC_2H_5$ is only 0.90 mV. The ζ potential variation signifies that the types of the colloidal particles in the two solutions are completely different. Since the Cl^- ions are difficult to remove in the calcination procedure, a higher temperature is needed to form the $NaNbO_3$ crystal. The XRD patterns of the samples (Fig. S4 in ESI†), which were obtained through the lower temperature calcinations of organic and inorganic coordinated polymer precursors, supply the obvious evidence of the two different growth mechanisms. Although the carbon materials are not oxidized completely, the $NaNbO_3$ crystal is generated at an oxidation temperature of 400 °C with the organic ligands. However, with the inorganic ligands, the $NaNbO_3$ crystal occupies only a portion of the products obtained from the 500 °C calcination. After the Cl^- ions are removed in the calcination, $NaNbO_3$–inorganic has a bare surface and orthorhombic $NaNbO_3$ is formed.

The H_2 evolutions from methanol aqueous solution (220 mL H_2O + 50 mL CH_3OH) over 0.5 wt% of Pt-loaded powder catalysts (0.3 g) under the irradiation of a full-arc Xe lamp ($\lambda > 300$ nm) are plotted in Fig. 4a. As mentioned previously, cubic $NaNbO_3$ has better photocatalytic performance than orthorhombic $NaNbO_3$ due to its unique electronic structure which benefits the generation and migration of photo-generated electrons and holes. In the H_2 evolution experiments, $NaNbO_3$–inorganic exhibits significantly lower activity (90 μmol h^{-1}) than $NaNbO_3$–organic (136 μmol h^{-1}). As $NaNbO_3$–organic and $NaNbO_3$–inorganic have different surface areas, the surface specific activities, which is the amount of product generated per surface area, are calculated for further comparison. The surface

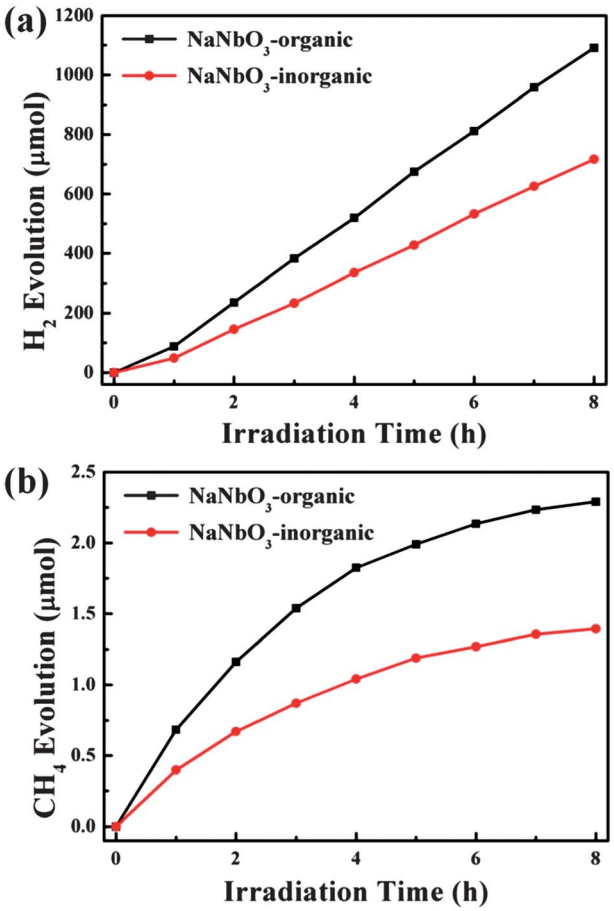

Fig. 4 (a) Photocatalytic H_2 evolution from aqueous methanol solution over $NaNbO_3$–inorganic and $NaNbO_3$–organic with 0.5 wt% Pt loading. (b) CH_4 evolution in gaseous phase reaction over $NaNbO_3$–inorganic and $NaNbO_3$–organic with 0.5 wt% Pt loading.

specific H_2 evolution rate over $NaNbO_3$–organic (4.95 μmol h^{-1} m^{-2}) is higher than that over $NaNbO_3$–inorganic (4.07 μmol h^{-1} m^{-2}). The higher H_2 evolution activity over $NaNbO_3$–organic is attributed to the crystal-structural diversity.

The photocatalytic properties of $NaNbO_3$–organic and $NaNbO_3$–inorganic were also verified in converting CO_2 into an organic product, CH_4. In the gaseous phase of CO_2 reduction, CH_4 is the main organic product, along with other organic and inorganic products.[31,32] The CO_2 photoreduction process mainly comprises the two reactions of reduction and oxidation. In the reduction course, the photo-generated electrons migrate to the Pt co-catalyst and there are a sequence of reducing reactions from CO_2 to CH_4 ($CO_2 + 2H^+ + 2e^- \rightarrow HCOOH$, $HCOOH + 2H^+ + 2e^- \rightarrow HCHO + H_2O$, $HCHO + 2H^+ + 2e^- \rightarrow CH_3OH$, $CH_3OH + 2H^+ + 2e^- \rightarrow CH_4 + H_2O$). In the oxidation process, the photo-generated holes transfer to the catalyst surface and oxidize H_2O to O_2 ($2H_2O + 4h^+ \rightarrow O_2 + 4H^+$).[33,34] Fig. 4b exhibits the CH_4 evolutions from gas phase CO_2 photoreduction over the $NaNbO_3$ samples with 0.5 wt% Pt-loading (0.1 g) under the irradiation of a full-arc Xe lamp ($\lambda > 300$ nm). The ratio of product generation rates for CO_2 photoreduction over the two samples ($NaNbO_3$–organic) : $NaNbO_3$–inorganic = 1.65) is higher than that for H_2 evolution ($NaNbO_3$–organic : $NaNbO_3$–inorganic = 1.51), suggesting that the surface area is more important for gas phase reaction than liquid phase reaction. With the same order as H_2 evolution, $NaNbO_3$–organic shows higher activity (0.286 μmol h^{-1}) in reducing CO_2 to CH_4 than $NaNbO_3$–inorganic (0.174 μmol h^{-1}). The surface specific CH_4 evolution rates show the clear difference of reaction activity between $NaNbO_3$–organic (10.4 nmol h^{-1} m^{-2}) and $NaNbO_3$–inorganic (7.9 nmol h^{-1} m^{-2}). Further investigation to confirm CH_4 is the product of CO_2 reduction was carried out by using $^{13}CO_2$. The result clearly verified that the organic product $^{13}CH_4$ was reduced from $^{13}CO_2$ (Fig. S2 in ESI†).

$NaNbO_3$ evolution with oxidation temperature

Cubic $NaNbO_3$ with enhanced photocatalytic performances was synthesized from the organic ligands. Nevertheless, it is still necessary to further enhance the photocatalytic activity. For this purpose, we tried to prepare the cubic $NaNbO_3$ photocatalyst at a temperature lower than 600 °C, so that the higher surface area and activity could be obtained.

According to the thermogravimetry (TG) and differential thermal analysis (DTA) (Fig. S5 in ESI†), the polymerized precursor was selectively oxidized over the temperature range from 500 to 900 °C with a 100 °C step. The crystallographic phases of the $NaNbO_3$ products were determined from their XRD patterns (Fig. 5). The $NaNbO_3$ samples oxidized at 500 and 900 °C crystallized in cubic and orthorhombic phases, respectively. All the peaks in these patterns could be indexed to the JCPDS database card numbers 075-2102 and 073-0803. As the oxidation temperature increases from 500 to 900 °C, the $NaNbO_3$ sample shows an obvious phase transition from cubic to orthorhombic phase. At the oxidation temperature of 500 and 600 °C, the samples keep the cubic structure; when the oxidation temperature rises to 700 °C, the orthorhombic phase is

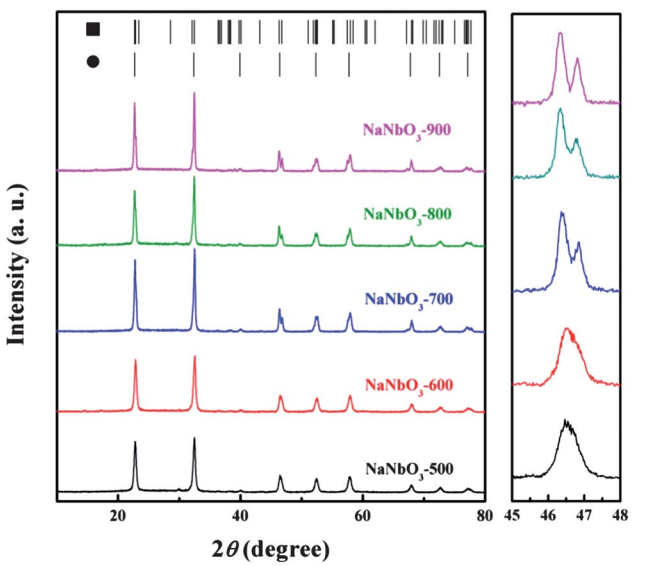

Fig. 5 XRD patterns of the oxidation temperature relative $NaNbO_3$ samples (■: orthorhombic; ●: cubic).

formed. The diffraction peak (2θ is about 46.5°) that distinguishes the cubic phase from the orthorhombic phase shows an obvious splitting as the oxidation temperature changes from 600 to 700 °C. The desorption of surface carbonate ions is considered as the impetus of the oxidation temperature driven phase transition in the FAPO procedure. Along with the upward evolution of the oxidation temperature, the bonding between the $NaNbO_3$ crystal and the surface coordinated carbonate ions is ruined and the crystal structure of $NaNbO_3$ reforms from cubic to orthorhombic consequently to reduce the surface energy Table 2.

Fig. 6a presents the H_2 evolutions from methanol aqueous solution over $NaNbO_3$ powder catalysts (0.3 g) with 0.5 wt% Pt loading under the irradiation of a full-arc Xe lamp ($\lambda > 300$ nm). As the crystal structure of $NaNbO_3$ remarkably affects the photocatalytic activity, the $NaNbO_3$ samples in cubic phase ($NaNbO_3$-500 and $NaNbO_3$-600) show higher H_2 evolution activities than those in orthorhombic phase ($NaNbO_3$-700, $NaNbO_3$-800, and $NaNbO_3$-900). In addition, the surface area is also an important factor that can greatly affect the photocatalytic efficiency. The larger surface area induces more active sites and a shorter migration distance, which would profit the photocatalytic reactions. For cubic $NaNbO_3$, $NaNbO_3$-500 (169 μmol h^{-1}) has a higher activity than $NaNbO_3$-600 (136 μmol h^{-1}) during the 8 hours of the H_2 evolution experiments. For orthorhombic $NaNbO_3$, the average H_2 evolution rates are 100, 78, and 63 μmol h^{-1} over 8 hours for $NaNbO_3$-700, $NaNbO_3$-800, and $NaNbO_3$-900, respectively. However, the surface specific H_2 evolution rates over the $NaNbO_3$ samples show the opposite order to the total H_2 evolution rates (4.01, 4.95, 8.06, 8.76 and 9.26 μmol h^{-1} m^{-2} over $NaNbO_3$-500, $NaNbO_3$-600, $NaNbO_3$-700, $NaNbO_3$-800 and $NaNbO_3$-900, respectively). The lower crystallinity and surface specific co-catalyst loading of the samples obtained at lower temperatures are considered as the explanation for this phenomenon. Fig. 6b exhibits the CH_4 evolutions from gas phase CO_2 photoreduction over the series of $NaNbO_3$ samples (0.1 g) loaded with 0.5 wt% of Pt under the irradiation of a full-arc Xe lamp ($\lambda > 300$ nm). With the increase of oxidation temperature, the total CH_4 evolution rate decreases, which shows the same order as H_2 evolution.

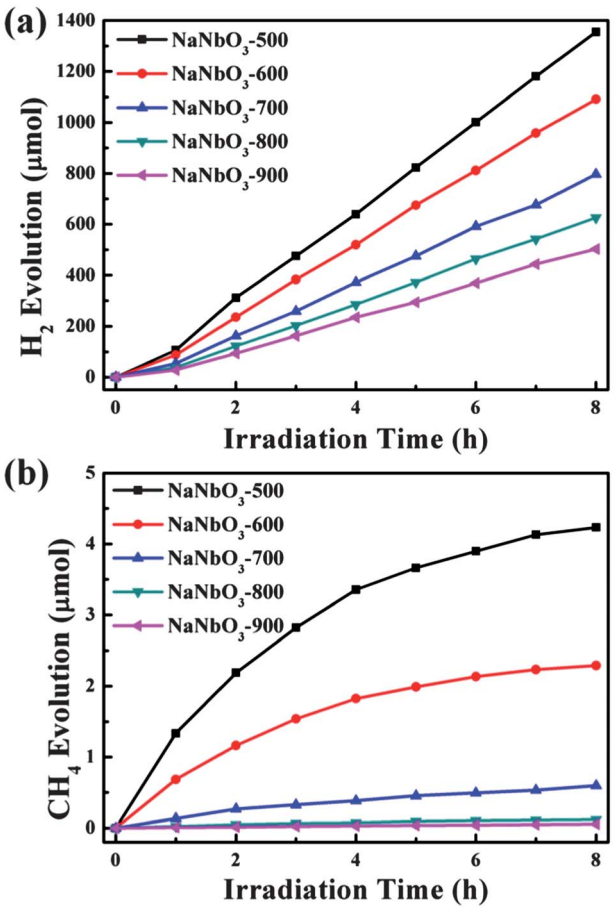

Fig. 6 (a) Photocatalytic H_2 evolution from aqueous methanol solution over the oxidation temperature relative $NaNbO_3$ samples with 0.5 wt% Pt loading. (b) CH_4 evolution in gaseous phase reaction over the oxidation temperature relative $NaNbO_3$ samples with 0.5 wt% Pt loading.

Table 2 Crystal structures of the oxidation temperature relative $NaNbO_3$ samples

Material	Crystal system	Lattice parameters (Å)	Surface area (m^2 g^{-1})
$NaNbO_3$-500	Cubic	$a = 3.8985(7)$	42.1
$NaNbO_3$-600	Cubic	$a = 3.897(1)$	27.5
$NaNbO_3$-700	Orthorhombic	$a = 5.515(1)$ $b = 5.571(1)$ $c = 15.524(2)$	12.4
$NaNbO_3$-800	Orthorhombic	$a = 5.5138(5)$ $b = 5.5690(7)$ $c = 15.523(1)$	8.9
$NaNbO_3$-900	Orthorhombic	$a = 5.513(1)$ $b = 5.570(2)$ $c = 15.519(2)$	6.8

$NaNbO_3$-500 shows the highest activity in reducing CO_2 to CH_4. The surface specific activities of reducing CO_2 to CH_4 are 12.6, 10.4, 6.0, 1.7 and 1.0 μmol h^{-1} m^{-2} over $NaNbO_3$-500, $NaNbO_3$-600, $NaNbO_3$-700, $NaNbO_3$-800 and $NaNbO_3$-900, respectively. The surface area has a more significant effect on the photocatalytic CO_2 reduction performance.

Conclusions

In conclusion, cubic and orthorhombic $NaNbO_3$ could be controllably synthesized at 600 °C *via* a surface coordination modulation using organic and inorganic starting reagents. The study of the crystal growth mechanism of cubic $NaNbO_3$ indicates that the organic ligands coordinated on the surface of the $NaNbO_3$ crystal lower its surface energy which induces the cubic $NaNbO_3$ product. In photocatalytic H_2 generation and CO_2 reduction, the $NaNbO_3$ sample prepared with organic ligands shows higher activities than that prepared with inorganic ligands because of the phase difference. Among the series of oxidation temperature dependant samples, the $NaNbO_3$ sample oxidized at 500 °C has the best photocatalytic performances in H_2 evolution and CO_2 reduction due to its cubic crystal structure

and higher surface area which were obtained from the lower-temperature oxidation of the organic ligand coordinated precursor. Our work evidences that surface chemical modulation *via* a coordination effect is able to control the crystal structure of an inorganic material and lower the formation temperature to obtain the product with larger surface area for a higher photocatalytic efficiency. The present study reveals that the surface chemistry of the material in the synthesis plays a significant role in its final crystallized phase and thus affects its photochemical performance.

Acknowledgements

This work was partially supported by the World Premier International Research Center Initiative on Materials Nanoarchitectonics, MEXT, Japan.

Notes and references

1 A. Fujishima and K. Honda, *Nature*, 1972, **238**, 37.
2 H. Tong, S. Ouyang, Y. Bi, N. Umezawa, M. Oshikiri and J. Ye, *Adv. Mater.*, 2012, **24**, 229.
3 X. B. Chen, S. H. Shen, L. J. Guo and S. S. Mao, *Chem. Rev.*, 2010, **110**, 6503.
4 G. Palmisano, E. Garcia-Lopez, G. Marci, V. Loddo, S. Yurdakal, V. Augugliaro and L. Palmisano, *Chem. Commun.*, 2010, **46**, 7074.
5 M. D. Hernandez-Alonso, F. Fresno, S. Suarez and J. M. Coronado, *Energy Environ. Sci.*, 2009, **2**, 1231.
6 U. Diebold, *Surf. Sci. Rep.*, 2003, **48**, 53.
7 D. Ravelli, D. Dondi, M. Fagnoni and A. Albini, *Chem. Soc. Rev.*, 2009, **38**, 1999.
8 A. L. Linsebigler, G. Q. Lu and J. T. Yates, *Chem. Rev.*, 1995, **95**, 735.
9 A. Fujishima, X. T. Zhang and D. A. Tryk, *Surf. Sci. Rep.*, 2008, **63**, 515.
10 L. A. Silva, S. Y. Ryu, J. Choi, W. Choi and M. R. Hoffmann, *J. Phys. Chem. C*, 2008, **112**, 12069.
11 S. Tokunaga, H. Kato and A. Kudo, *Chem. Mater.*, 2001, **13**, 4624.
12 S. X. Ouyang, Z. S. Li, Z. Ouyang, T. Yu, J. H. Ye and Z. G. Zou, *J. Phys. Chem. C*, 2008, **112**, 3134.
13 S. K. Mishra, N. Choudhury, S. L. Chaplot, P. S. R. Krishna and R. Mittal, *Phys. Rev. B: Condens. Matter Mater. Phys.*, 2007, **76**, 024110.
14 S. K. Mishra, R. Mittal, V. Y. Pomjakushin and S. L. Chaplot, *Phys. Rev. B: Condens. Matter Mater. Phys.*, 2011, **83**, 134105.
15 K. E. Johnston, C. C. Tang, J. E. Parker, K. S. Knight, P. Lightfoot and S. E. Ashbrook, *J. Am. Chem. Soc.*, 2010, **132**, 8732.
16 Y. Shiratori, A. Magrez, J. Dornseiffer, F. H. Haegel, C. Pithan and R. Waser, *J. Phys. Chem. B*, 2005, **109**, 20122.
17 X. K. Li, Z. J. Zhuang, W. Li and Q. Li, *Catal. Lett.*, 2012, **142**, 901.
18 H. F. Shi, T. Z. Wang, J. Chen, C. Zhu, J. H. Ye and Z. G. Zou, *Catal. Lett.*, 2011, **141**, 525.
19 K. Saito and A. Kudo, *Inorg. Chem.*, 2010, **49**, 2017.
20 G. Q. Li, T. Kako, D. F. Wang, Z. G. Zou and J. H. Ye, *J. Phys. Chem. Solids*, 2008, **69**, 2487.
21 P. Li, S. X. Ouyang, G. C. Xi, T. Kako and J. H. Ye, *J. Phys. Chem. C*, 2012, **116**, 7621.
22 N. Zhang, S. X. Ouyang, T. Kako and J. H. Ye, *Chem. Commun.*, 2012, **48**, 1269.
23 G. R. Patzke, Y. Zhou, R. Kontic and F. Conrad, *Angew. Chem., Int. Ed.*, 2011, **50**, 826.
24 D. R. Modeshia and R. I. Walton, *Chem. Soc. Rev.*, 2010, **39**, 4303.
25 G. Xi, S. Ouyang and J. Ye, *Chem.–Eur. J.*, 2011, **17**, 9057.
26 W. H. Liu, H. Wang and K. C. Li, *J. Sol-Gel Sci. Technol.*, 2010, **55**, 229.
27 M. A. Bollinger and M. A. Vannice, *Appl. Catal., B*, 1996, **8**, 417.
28 M. A. Butler, *J. Appl. Phys.*, 1977, **48**, 1914.
29 M. Sedlar and M. Sayer, *J. Sol-Gel Sci. Technol.*, 1995, **5**, 27.
30 M. Yoshino and M. Kakihana, *Chem. Mater.*, 2002, **14**, 3369.
31 N. Zhang, S. X. Ouyang, P. Li, Y. J. Zhang, G. C. Xi, T. Kako and J. H. Ye, *Chem. Commun.*, 2011, **47**, 2041.
32 S. C. Yan, S. X. Ouyang, J. Gao, M. Yang, J. Y. Feng, X. X. Fan, L. J. Wan, Z. S. Li, J. H. Ye, Y. Zhou and Z. G. Zou, *Angew. Chem., Int. Ed.*, 2010, **49**, 6400.
33 M. Mikkelsen, M. Jorgensen and F. C. Krebs, *Energy Environ. Sci.*, 2010, **3**, 43.
34 G. Centi, S. Perathoner, G. Wine and M. Gangeri, *Green Chem.*, 2007, **9**, 671.